Society of Medical Education & Research

2026, Volume 6, Issue 1, Page No: 271-288
ISSN: 3108-4834

Archive of International Journal of Cancer and Allied Science

A LINC00922–SIRT3 Axis Regulates H3K27 Crotonylation-Mediated ETS1 Activation to Drive Colorectal Cancer Metastasis

Daniel Fischer[1]*, Laura Meier[1], Stefan Koch[2], Thomas Braun[3]

[1]Department of Colorectal Cancer Metastasis and Long Noncoding RNA, Faculty of Medicine, University of Freiburg, Freiburg, Germany.
[2]Department of Histone Crotonylation and Epigenetic Regulation, Faculty of Medicine, Technical University of Munich, Munich, Germany.
[3]Department of ETS1 Activation and Tumor Progression, Faculty of Medicine, University of Kiel, Kiel, Germany.

***E-mail** ✉ daniel.fischer@pharmazie.uni-freiburg.de

Abstract

Lysine crotonylation (Kcr) is elevated in colorectal cancer (CRC) tissues, yet its functional significance in disease progression remains unclear. This investigation aimed to determine the specific contribution and molecular pathway of crotonylation at lysine 27 on histone H3 (H3K27cr) in driving CRC metastasis. Immunohistochemical staining was applied to assess the relationship between H3K27cr expression and metastatic features in CRC. Loss-of-function and gain-of-function experiments were carried out both in vitro and in vivo to evaluate the impact of LINC00922 on CRC metastatic potential. Single-cell RNA sequencing combined with immunoprecipitation-based approaches was used to delineate how LINC00922 influences CRC metastasis by modulating H3K27cr. In clinical specimens, H3K27cr was markedly increased in metastatic CRC tissues and showed a strong positive association with more advanced disease stages. Functionally, depletion of LINC00922 substantially reduced the migratory ability of CRC cells in culture and in animal models. Notably, supplementation with NaCr reversed the impaired migration and invasion observed in LINC00922-deficient cells by restoring H3K27cr levels. At the mechanistic level, LINC00922 stimulated cellular invasion and motility by enhancing H3K27cr-dependent expression of cell adhesion molecules (CAMs) within epithelial cells. Importantly, LINC00922 bound to sirtuin 3 (SIRT3) and interfered with its association at the ETS1 promoter. Consequently, this interaction increased H3K27cr enrichment at the ETS1 promoter, thereby upregulating ETS1 transcriptional activity. The present work identifies a previously unrecognized mechanism whereby H3K27cr, under the control of LINC00922, promotes metastatic spread in CRC. These insights advance current understanding of histone crotonylation's role in CRC metastasis.

Keywords: Colorectal cancer, Metastasis, LINC00922, H3K27cr, SIRT3

Introduction

Lysine crotonylation (Kcr), a post-translational modification identified relatively recently, occurs in both human and mouse cells [1]. This modification participates in diverse biological processes, including stem cell differentiation [2], spermatogenesis [3], acute kidney injury [4], HIV latency [5], autophagy [6], DNA repair [7], and tumor development [8]. The key substrate donor, crotonyl-CoA, critically governs intracellular crotonylation abundance. Histone crotonylation reaches its highest abundance in colonic tissue relative to other organs [9], a phenomenon potentially explained by the abundance of short-chain fatty acids (SCFAs) generated by intestinal microbiota, which boost crotonyl-CoA availability [10]. Crotonylation modifications are notably more abundant in colon cancer specimens than in neighboring non-malignant tissue. However, the underlying causes of this upregulation in CRC and its

Access this article online https://smerpub.com/

Received: 18 April 2026; **Accepted:** 23 June 2026

How to cite this article: Fischer D, Meier L, Koch S, Braun T. A LINC00922–SIRT3 Axis Regulates H3K27 Crotonylation-Mediated ETS1 Activation to Drive Colorectal Cancer Metastasis. Arch Int J Cancer Allied Sci. 2026;6(1):271-88. https://doi.org/10.51847/1A8gjyEXuQ

potential influence on tumor initiation and advancement remain largely unresolved. Existing evidence primarily connects non-histone crotonylation events to CRC pathogenesis. For example, Liao *et al*. [11] demonstrated that gut microbiota-derived crotonic acid (CA) enhances CRC cell proliferation by crotonylating P53 at Ser46. Likewise, Kcr modification of α-enolase at residue K420 augments CRC cell proliferation, motility, and invasiveness [12].

Crotonyl-CoA generated in mitochondria can translocate to the nucleus and induce histone crotonylation. Prior research by Xu *et al*. [13] established that BRD4 drives prostate cancer (PCa) cell migration and invasion through histone crotonylation pathways. Despite these observations, the precise role of histone crotonylation in CRC progression remains incompletely understood. Our earlier experiments indicated a significant decline in H3K27cr during DNA damage responses in HCT116 cells [14]. Given the intimate connection between DNA damage responses and metastatic behavior in CRC, H3K27cr is likely to play an important role in metastasis. Histone crotonylation represents a reversible modification governed by the balanced activities of crotonyltransferases and decrotonylases. SIRT3 resides predominantly in the mitochondrial matrix and is widely characterized as an NAD+-dependent deacetylase. Recent findings by Wei *et al*. [15] revealed that pharmacological inhibition of SIRT3 using NAM for 24 hours leads to elevated histone crotonylation. Complementary work by Bao *et al*. [16] confirmed SIRT3's role as a histone decrotonylase capable of modulating gene expression patterns through changes in lysine crotonylation. It demonstrated its enzymatic activity toward crotonylated histone substrates. Additional evidence indicates that SIRT3 is nuclear localized and participates in physiologic and disease-related processes by regulating core histone modifications. Nonetheless, the mechanisms that direct SIRT3 to specific chromatin regions remain poorly characterized.

Long noncoding RNAs (lncRNAs) have emerged as important mediators that recruit histone-modifying enzymes to defined genomic locations. For instance, EPB41L4A-AS1 associates with GCN5 to facilitate its targeting to promoters of genes involved in glucose metabolism [17]. Similarly, NEAT1 interacts with the P300/CBP complex to modulate H3K27 crotonylation at promoters of genes regulating endocytosis [18]. At present, direct physical interactions between lncRNAs and SIRT3 have not been documented.

LINC00922 is known to enhance proliferative, migratory, and invasive capacities across multiple malignancies, including colorectal, lung, gastric, ovarian, and liver cancers. Prior reports suggest that LINC00922 operates both as a competing endogenous RNA for microRNAs and as a recruiter of DNA methyltransferases (DNMTs) to promoters of metastasis-associated genes, thereby altering their transcriptional output [19, 20]. In our analyses, H3K27cr and LINC00922 showed concordant upregulation in CRC samples, with particularly high expression in distant metastases compared with primary tumors. Gene set enrichment analysis (GSEA) further linked LINC00922 expression to gene signatures characterized by H3K27cr promoter occupancy. Experimental data confirmed LINC00922's involvement in CRC cell invasion and migration. At the molecular level, LINC00922 physically associates with SIRT3, restricting its recruitment to the ETS1 promoter. This interference increases H3K27cr deposition at the ETS1 regulatory region, thereby enhancing ETS1 transcription. These molecular events collectively accelerate CRC cell invasion and migration in both cell culture and animal models. Overall, the data position H3K27cr as a central regulator of metastatic progression in CRC.

Materials and Methods

Cell culture

Several human colorectal cancer (CRC) cell lines—HCT116 (TCHu 99), LoVo (TCHu 82), DLD-1 (TCHu134), SW620 (TCHu101), and SW480 (SCSP-5033)—were obtained from the Cell Bank of the Chinese Academy of Sciences (Shanghai, China). The human normal colorectal epithelial cell line FHC (CRL-1831) was sourced from the American Type Culture Collection (Manassas, VA, USA). HCT116, LoVo, DLD-1, SW480, and FHC cells were grown in Dulbecco's modified Eagle medium (DMEM) (Bio-Channel, Cat. No: BC-M-005) supplemented with 10% fetal bovine serum (FBS) (ExCell Bio, Cat. No: FSP500) and 1% antibiotics (Vicmed, Cat. No: VC2003). SW620 cells were maintained in RPMI 1640 medium (Bio-Channel, Cat. No: BC-M-017) with 10% FBS and 1% antibiotics. All cultures were kept at 37 °C in a humidified incubator containing 5% CO_2.

Transfection and lentiviral transduction

siRNAs were chemically synthesized by Integrated Biotech Solutions (Shanghai, China), while expression plasmids were acquired from Hebio (Shanghai, China) or YouBio (Hunan, China). Transient transfection of siRNAs and plasmids was conducted according to the suppliers' recommended protocols with siLentFect lipid reagent (Bio-Rad, Cat. No: 1,703,361) and liposomal transfection reagent (YEASEN, Cat. No: 40802ES08), respectively. An sh-LINC00922 construct was generated and packaged into lentiviral vectors by GenePharma (Shanghai, China). Stable knockdown of LINC00922 in HCT116 cells was established through lentiviral transduction, followed by selection of successfully transduced cells using 4 μg/mL puromycin (Beyotime, Cat. No: ST551-10 mg) over two weeks.

Bioinformatics analysis

Original clinical and genomic datasets were retrieved from the UCSC Xena browser (https://xena.ucsc.edu) and the Gene Expression Omnibus (GEO; https://www.ncbi.nlm.nih.gov/geo/). Comparisons of LINC00922 and H3K27cr expression between two independent sample groups were performed with the Mann-Whitney U test. Differences across more than two groups were evaluated by one-way analysis of variance (ANOVA). Patient survival outcomes were assessed via Kaplan-Meier survival analysis. The chi-square test was applied to examine the distribution pattern of LINC00922 between cytoplasmic and nuclear compartments. Pearson correlation analysis was used to determine the relationship between LINC00922 and ETS1 expression levels in CRC tissues. Biological pathway enrichment was explored using KEGG analysis. A meta-analysis was additionally conducted to investigate the link between LINC00922 expression and metastatic progression in CRC.

Gene set enrichment analysis

GSEA was executed with the fgsea package (version 1.16.0) in the R statistical environment [21]. TCGA CRC samples were classified into high- and low-expression groups based on the median LINC00922 expression level. Relevant ChIP-seq profiles for H3K27cr along with additional crotonylation-associated gene sets were obtained from the GEO database for this analysis. Gene ranking was determined by fold-change values generated using the edgeR package (version 3.32.1) [22].

Differential expression analysis

Differentially expressed lncRNAs between normal colorectal and CRC tissues were identified through the edgeR package. Gene expression matrices were downloaded from the UCSC Xena database. Samples were categorized as either normal or tumor tissues. lncRNAs showing $|\text{fold-change}| \geq 2$ and * $P < 0.05$ were selected and visualized as heatmaps.

ScRNA-seq analysis

Single-cell RNA-seq datasets from GSE196964, GSE221575, and samples GSM7058756 to GSM7058761 (four primary and two liver metastatic CRC tissues) within GSE225857 were acquired from the GEO database. Subsequent processing was carried out in R using the Seurat, presto, dplyr, msigdbr, and tibble packages. Batch effect correction was achieved by identifying integration anchors with the FindIntegrationAnchors function and merging datasets via IntegrateData. Cell-type markers were detected with FindAllMarkers, and annotations were assigned using the CellMarker 2.0 database. Gene set enrichment within individual cell types was evaluated using fgsea, and the results were visualized with ggplot2. The overall analytical pipeline was adapted from the methodology outlined by Wu *et al*. [23].

Transwell assay

Cells were plated in Transwell inserts with 8 μm pore-size membranes (Corning, Cat. No: 3422), either uncoated or pre-coated with Matrigel (Corning, Cat. No: 356234). The upper chamber received 200 μL of serum-free medium containing the cell suspension, while the lower chamber received 600 μL of medium containing 10% FBS. After incubation for 24 and 48 hours, cells that had traversed the membrane were fixed with 4% paraformaldehyde and stained with 0.1% crystal violet. Images were acquired with an Olympus microscope at ×100 magnification and subsequently quantified in ImageJ.

Wound healing assay

LoVo cells were initially plated in six-well plates and allowed to grow until reaching approximately 95% confluence. A sterile pipette tip (200 μL) was employed to generate a uniform scratch wound across the monolayer surface. Following removal of floating cells by gentle washing, the remaining cells were incubated in fresh, serum-free medium. Images documenting wound

progression were acquired at 0 h and 48 h using a Nikon digital camera (Nikon, Tokyo, Japan) at ×100 magnification. The extent of wound closure was subsequently determined by measuring changes in wound area.

Western blot

Whole-cell protein extracts were prepared by lysing cells in a buffer containing 50 mM Tris-HCl (pH 8.0), 4 M urea, and 1% Triton X-100, with the addition of protease inhibitors. Protein concentrations in the lysates were measured using a BCA assay kit (KeyGEN BioTECH, Cat. No: KGP902). Proteins were then separated by molecular weight via SDS-PAGE electrophoresis and transferred to nitrocellulose membranes. After blocking the membranes in 5% skim milk for 2 h, they were incubated overnight at 4 ℃ with specific primary antibodies, followed by a 1 h incubation with corresponding secondary antibodies. Primary antibodies included anti-ETS1 (Beyotime, Cat. No: AF6812, 1:1,000), anti-E-Cad (ABclonal, Cat. No: A20798, 1:2,000), anti-Vimentin (Proteintech, Cat. No: 10366-1-AP, 1:2,000), anti-Snail1 (Proteintech, Cat. No: 13099-1-AP, 1:1,000), anti-SIRT3 (Santa Cruz, Cat. No: sc-365,175, 1:200), anti-H3K27cr (PTM BIO, Cat. No: PTM-545RM, 1:1,000), anti-GAPDH (Proteintech, Cat. No: 60004-1-Ig, 1:10,000), anti-H3 (Proteintech, Cat. No: 17168-1-AP, 1:10,000). Secondary antibodies were anti-rabbit IgG (SAB, Cat. No: L3012, 1:10,000) and anti-mouse IgG (SAB, Cat. No: L3032, 1:10,000). Signal intensities of the resulting bands were quantified using ImageJ.

Quantitative real-time PCR

Total RNA extracted from cells and tissue specimens using TRIzol reagent was converted to cDNA with the SweScript RT I First Strand cDNA Synthesis Kit (Servicebio, Cat. No: G3330-50). Quantitative real-time PCR amplification was carried out utilizing 2×SYBR Green qPCR Master Mix (High ROX) (Servicebio, Cat. No: G3322-05). All samples were analyzed in triplicate, and relative gene expression was normalized to GAPDH and calculated using the $2^{-\Delta\Delta Ct}$ method.

Immunofluorescence staining

For immunofluorescence detection, antibodies specific to ETS1 (1:50), H3K27cr (1:100), and SIRT3 (1:50) were utilized. Cells were cultured on coverslips for 24 h before processing. After washing three times with PBS, fixation occurred in cold methanol for 5 min. Blocking was performed with 3% bovine serum albumin (BSA) for 1 h at room temperature, followed by a 2 h incubation with primary antibodies. Secondary labeling was achieved by incubating the samples for 1 h at room temperature in 3% FBS containing Alexa Fluor 594-conjugated Goat Anti-Rabbit IgG(H+L) (Vicmed, Cat. No: VA027, 1:100) and/or Alexa Fluor 488-conjugated Affinipure Goat Anti-Mouse IgG(H+L) (Vicmed, Cat. No: VA1021, 1:100). Nuclear visualization was enabled by DAPI staining. Slides were examined using a fluorescence microscope or STELLARIS 5 confocal fluorescence microscope (Leica).

Chromatin immunoprecipitation (ChIP-seq and ChIP-qPCR) assays

Formaldehyde (1%) was used to cross-link proteins to DNA in intact cells, after which cells were resuspended in ChIP lysis buffer (50 mM Tris-HCl (pH 8.0), 5 mM EDTA, 0.1% deoxycholate, 1% Triton X-100, 150 mM NaCl, and 20 μL/mL PIC). After 10 min of sonication, the lysates were centrifuged to remove debris. The cleared supernatants were then incubated for 4 h with target antibodies bound to Protein A/G beads. Anti-H3K27cr and anti-SIRT3 antibodies were applied in the immunoprecipitation step, with rabbit IgG (Beyotime, Cat. No: A7016) and mouse IgG (Bioworld, Cat. No: BD0050) acting as negative controls. After three washes, the DNA-protein complexes were processed to isolate DNA, which was subsequently analyzed by qRT-PCR or sent to Orizymes (Shanghai, China) for sequencing.

Cell fractionation assay

Cytoplasmic and nuclear RNA were separated using the nuclear and cytoplasmic protein extraction kit (Beyotime, Cat. No: P0027). Cytoplasmic extraction reagent A was supplemented with PMSF and RRI before use. Cells were lysed on ice for 15 min with pre-cooled reagents A and B. The lysate was centrifuged to yield a supernatant for cytoplasmic RNA isolation. The nuclear pellet was further resuspended in reagents A and B, incubated on ice for 45 min, and washed three times with PBS to eliminate cytoplasmic contaminants. Nuclear RNA was extracted from the final pellet with TRIzol reagent.

RNA immunoprecipitation assay

Collected cells were lysed in RIP buffer (10 mM KCl, 5 mM $MgCl_2$, 10 mM HEPES (pH 7.0), 0.5% NP-40, 1 mM

DTT, 100 U/mL RRI, 20 µL/mL protease inhibitor, and 2 mM vanadyl ribonucleotide complex). The lysates were combined with 3 µg of IP-grade anti-SIRT3 antibody and incubated overnight at 4 °C, with mouse IgG serving as the control. Protein A/G beads (40 µL) were then added for a 4 h incubation. The immunoprecipitated RNA complexes were recovered, purified, and analyzed through qRT-PCR.

Fluorescent in situ hybridization (RNA-FISH) and immunofluorescence microscopy

The Cyanine 5-labeled LINC00922 RNA probe was acquired from Integrated Biotech Solutions (Shanghai, China). Briefly, cells were plated onto coverslips placed in a 12-well plate. The next day, the coverslips were rinsed three times with PBS. Cells were then permeabilized using CSK buffer on ice for 5 min, followed by fixation in 4% paraformaldehyde for 10 min. After successive dehydration steps in 80%, 95%, and 100% ethanol (3 min each), the samples were hybridized with the LINC00922 probe at 37 °C overnight within a humidified, light-protected chamber. Coverslips were subsequently washed three times with freshly prepared 50% formamide in 2 × SSC buffer at 42 °C for 5 min per wash. Cells were blocked with 1% BSA for 15 min and incubated with anti-SIRT3 antibody (1:50) for 45 min. Specimens were finally counterstained with DAPI, mounted, and visualized under a STELLARIS 5 confocal fluorescence microscope (Leica).

Immunohistochemistry (IHC)

Colorectal tissue specimens, including tumor samples from 45 patients and matched adjacent normal tissues from 14 patients, were sourced from Shanghai Outdo Biotech Company (Shanghai, China). Among the 45 tumor samples, 10 were distant metastatic colorectal cancer tissues, 16 were primary colorectal cancer tissues, 11 were colorectal adenoma tissues, and 8 were lymph node-positive tissues. Tissue sections were deparaffinized twice in xylene for 15 min each and rehydrated through a graded ethanol series (100% ethanol twice for 7 min each, followed by 90%, 80%, and 70% ethanol for 5 min each). Antigen retrieval was performed in 0.01 M citrate buffer, and endogenous peroxidase was inactivated with 3% hydrogen peroxide. After blocking with BSA, sections were incubated overnight at 4 °C with anti-H3K27cr antibody (1:100), followed by a 30-min incubation at room temperature with HRP-conjugated secondary antibody (SAB, Cat. No: L3012, 1:100). Sections were then dehydrated, mounted with neutral resin, and observed microscopically. Two independent observers performed blinded evaluation of the staining.

H3K27cr expression levels were assessed via the histochemistry score (H-score), obtained by multiplying staining intensity (graded 0–3: 0 = absent, 1 = weak, 2 = moderate, 3 = strong) by the percentage of positively stained cells (0–100%). This produced H-scores ranging from 0 to 300. Continuous H3K27cr levels were compared across groups in **Figures 1b and 1d**. For **Tables 1 and 2**, the percentage of positive cells was converted to a 0–4 scale: 0 (< 5%), 1 (5–25%), 2 (25–50%), 3 (50–75%), and 4 (> 75%). The product of intensity and area grades yielded a composite score ranging from 0 to 12, with scores above 6 indicating high H3K27cr expression. Statistical significance was determined using the four-table chi-square test.

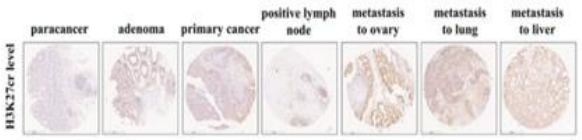

a)

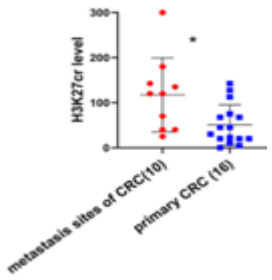

b)

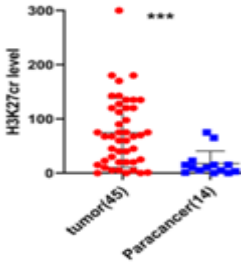

c)

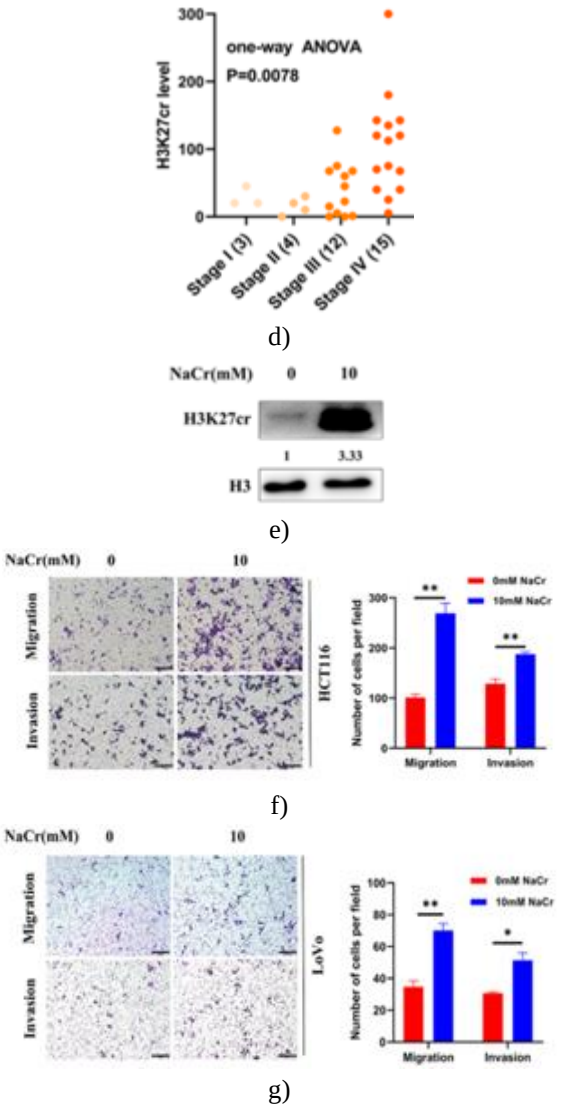

Figure 1. Clinical evidence indicating an association between H3K27cr and metastasis in colorectal cancer (CRC)

(a) Representative immunohistochemistry images of H3K27cr expression in different CRC tissue categories. Scale bar, 500 μm. (b–c) Statistical comparisons of H3K27cr levels across CRC tissue types using Mann-Whitney U tests (b–c) and one-way ANOVA (d). The 45 tumor cases analyzed in Figure (c) consisted of 10 distant metastatic colorectal cancer samples, 16 primary colorectal cancer samples, 11 colorectal adenoma samples, and 8 positive lymph node samples. (e) Western blot analysis showing H3K27cr levels in HCT116 cells following treatment with 10 mM NaCr for 48 h. Values below the H3K27cr bands indicate the relative ratio of H3K27cr to total H3 (normalized to the control), as determined using ImageJ2. (f–g) Representative images from Transwell invasion and migration assays in HCT116 (f) and LoVo (g) cells treated with 10 mM NaCr for 48 h (left panels). Scale bar, 200 μm. Quantitative data from three randomly selected fields are shown (right panels). Results are expressed as means ± SD. * $P < 0.05$, ** $P < 0.01$, *** $P < 0.001$ by unpaired, two-tailed Student's t-test.

Table 1. Correlation between H3K27cr level and clinicopathological characteristics.

Clinicopathological parameter	Category	Low H3K27cr expression	High H3K27cr expression	Total	χ^2 statistic	P-value
Sex	Male	20	6	26	0.56	0.45
	Female	12	6	18		
	NA			1		
Age (years)	≤54	14	4	18	0.007	0.93
	>54	15	4	19		
	NA			8		
Histological grade	G1–3	14	4	18	5.08	0.024
	G4	3	6	9		
	NA			18		
Tumor size	≤5 cm	16	3	19	0.17	0.68
	>5 cm	11	3	14		
	NA			12		
T stage	T2	3	0	3	0.71	0.40
	T3	8	2	10		
	NA			32		
N stage	N0	7	0	7	0.90	0.34
	N1/N2	15	2	17		
	NA			21		
M stage	M0	18	1	19	7.99	0.005
	M1	8	7	15		
	NA			11		
TNM stage	I–III	18	1	19	7.99	0.005
	IV	8	7	15		
	NA			11		

Table 2. Differential level of H3K27cr in cancer and paracancer tissues

Tissue type	Low H3K27cr expression	High H3K27cr expression	Sample size (*n*)	χ^2 statistic	P-value
Tumor tissue	32	13	45	5.19	0.023
Adjacent non-tumor tissue	14	0	14		

Animal experiment

To examine the involvement of LINC00922 in colorectal cancer (CRC) metastasis, an experimental lung metastasis model was established using nude mice. BALB/c nude mice supplied by GemPharmatech (Nanjing, China) were randomly allocated into two experimental groups (n = 8 per group). Each mouse received a tail vein injection of $3 \times 10^{\wedge 6}$ HCT116 cells, either unmodified (control) or carrying a stable LINC00922 knockdown. During the study, four mice in the control group succumbed. Five weeks post-injection, the surviving animals were euthanized (four from the control group and eight from the sh-LINC00922 group). Lungs harboring visible tumor nodules were excised, imaged, and analyzed quantitatively.

Statistical analysis

All experiments were repeated independently three times, and quantitative results are reported as mean ± SD. Statistical analyses were conducted using SPSS version 22.0, and graphical representations were prepared using GraphPad Prism version 8.0. Comparisons between two groups were performed with unpaired two-tailed Student's t-test, Mann-Whitney U test, or Chi-square test, as appropriate. For comparisons across multiple groups, a one-way ANOVA was used. Pearson's correlation analysis assessed relationships between variables. Statistical significance was defined as * $P < 0.05$.

Results and Discussion

Clinically, H3K27cr level is associated with metastasis of CRC tissues

H3K27cr expression was evaluated by immunohistochemistry in colorectal tumor specimens from 45 patients and corresponding adjacent tissues from 14 patients. The analysis revealed markedly elevated H3K27cr levels in tissues from distant metastatic sites **(Figures 1a and 1b)**. Significant associations were also detected between H3K27cr expression and tumor grade, M stage, and TNM stage **(Table 1)**. Compared with adjacent non-tumorous tissues, CRC tissues exhibited substantially higher H3K27cr expression **(Figure 1c and Table 2)**. Furthermore, H3K27cr levels were higher in stage III and IV tumors than in stage I and II tumors **(Figure 1d)**. Given its association with distant metastasis, it was postulated that H3K27cr may actively contribute to metastatic progression. NaCr augments histone crotonylation by directly supplying crotonyl-CoA [24]. Consistent with this, culturing HCT116 cells in medium containing 10 mM NaCr effectively raised intracellular H3K27cr levels **(Figure 1e)**. This treatment also significantly enhanced the invasive and migratory abilities of CRC cells **(Figures 1f and 1g)**. Taken together, these data support the conclusion that H3K27cr promotes metastasis in CRC.

LINC00922 is associated with H3K27cr level, metastasis and poor prognosis in CRC

Given that lncRNAs have been implicated in the control of histone crotonylation [17], the potential connection between H3K27cr and lncRNAs was explored. Differential expression analysis of lncRNAs in normal and CRC tissues from the TCGA dataset identified several lncRNAs that were dysregulated in tumors. ChIP-seq experiments using an H3K27cr-specific antibody were then performed in HCT116 cells to identify genes whose promoters were occupied by H3K27cr. Gene set enrichment analysis (GSEA) comparing these genes with the dysregulated lncRNAs showed significant enrichment in CRC samples characterized by high LINC00922 expression, along with eight additional lncRNAs **(Figure 2a)**. In contrast, no notable associations were observed with promoters marked by H3K9cr or H3K18cr. Overexpression of LINC00922 resulted in a clear increase in H3K27cr levels **(Figure 2b)**. These observations point to a specific link between LINC00922 and H3K27cr.

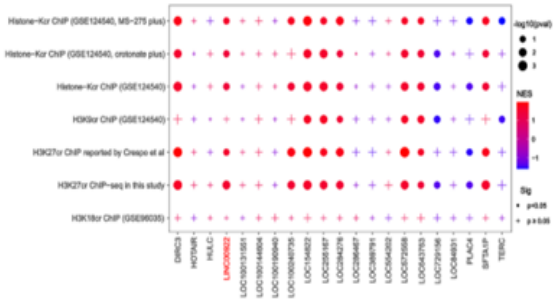

a)

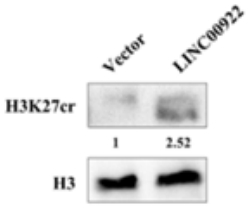

b)

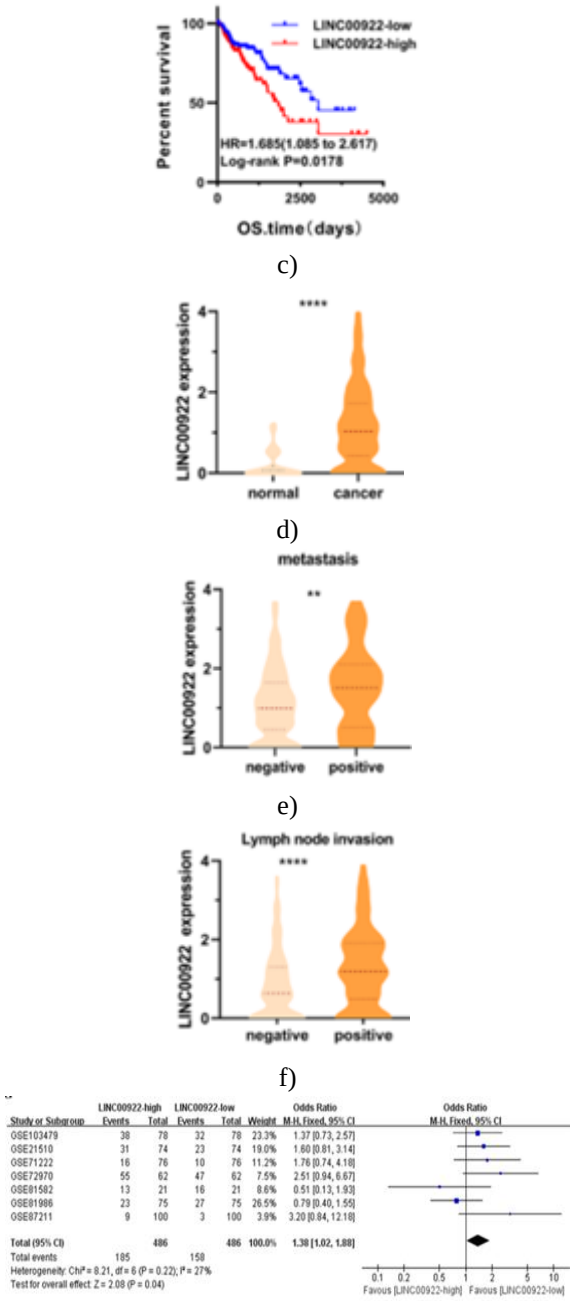

Figure 2. Association of LINC00922 with CRC metastasis and poor prognosis

(a) Enrichment plot of genes bearing promoters occupied by histone crotonylation among multiple dysregulated lncRNAs. GSEA evaluated statistical significance. Dots denote $P < 0.05$, and symbols denote $P \geq 0.05$. Red dots indicate positive correlation with the lncRNA, whereas blue dots indicate negative correlation. Point size reflects the negative base-10 logarithm of the p-value. NES: normalized enrichment score. (b) Immunoblot analysis of H3K27cr levels in HCT116 cells 48 h after transfection with a LINC00922 expression plasmid. Numbers beneath the H3K27cr bands represent the H3K27cr/H3 ratio in treated groups relative to control, as quantified by ImageJ2. (C) Kaplan-Meier survival analysis of the relationship between LINC00922 expression and overall survival (OS, n = 326) in the TCGA CRC cohort. (D) Mann-Whitney U test comparing LINC00922 expression in normal and CRC tissues from the TCGA database. **** $P < 0.0001$, (E, F) Mann-Whitney U analysis of LINC00922 levels in TCGA CRC samples according to distant metastasis status (E) or lymph node invasion status (F). ** $P < 0.01$, ****$P < 0.0001$. (G) Meta-analysis examining the association between LINC00922 expression and distant metastasis across CRC samples (n = 972) from the GEO database.

Further clinical evaluation in the TCGA CRC cohort demonstrated that elevated LINC00922 expression correlated with reduced patient survival **(Figure 2c)**. LINC00922 levels were significantly higher in tumor tissues than in normal colorectal tissues **(Figure 2d)**. Similar upregulation was observed in multiple CRC cell lines relative to normal colorectal epithelial cells. Patients with distant metastasis or lymph node involvement displayed higher LINC00922 expression than those without **(Figures 2e and 2f)**. A meta-analysis of GEO datasets confirmed that high LINC00922 expression was associated with increased risk of distant metastasis (odds ratio (OR) = 1.38 (95% CI: 1.02 ~ 1.88, Z = 2.08, P = 0.04)) **(Figure 2g)**. Overall, these findings indicate that elevated LINC00922 expression is associated with increased metastatic potential and unfavorable clinical outcomes in CRC patients.

LINC00922 accelerates invasion and migration of CRC cells

Additional experiments were conducted to clarify how LINC00922 contributes to CRC metastasis by assessing its influence on the invasive and migratory behaviors of CRC cells. Knockdown of LINC00922 expression substantially impaired the invasion and migration abilities of these cells. In contrast, ectopic overexpression of LINC00922 markedly enhanced these processes **(Figures 3a and 3b)**. Similar findings were obtained in wound healing assays. The role of LINC00922 in metastatic spread was further examined in an animal model. HCT116 cells with stable LINC00922 knockdown were introduced into nude mice

through tail vein injection. This genetic intervention led to a pronounced decrease in pulmonary metastatic nodule formation **(Figure 3c)**. During the animal study, four mice in the sh-NC control group died. Among the remaining animals, the four sh-NC mice developed a total of 27 metastatic lung nodules, averaging 6.75 per mouse. In the sh-LINC00922 group, eight mice yielded a total of 20 metastatic nodules, averaging 2.5 nodules per mouse **(Figure 3d)**. Western blot analysis indicated that depletion of LINC00922 caused notable downregulation of several epithelial-mesenchymal transition (EMT) markers, such as Vimentin and Snail1. Conversely, increased expression of LINC00922 upregulated these proteins **(Figures 3e-3g)**. Overall, the data strongly indicate that LINC00922 drives the invasive and migratory phenotypes of CRC cells.

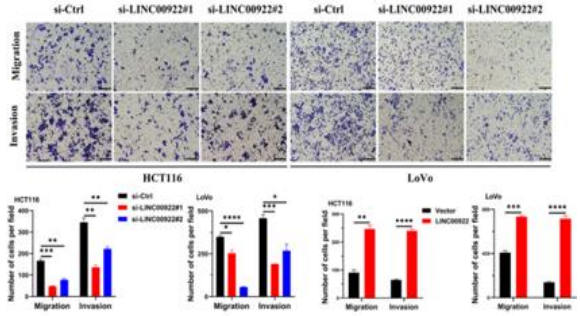

a)

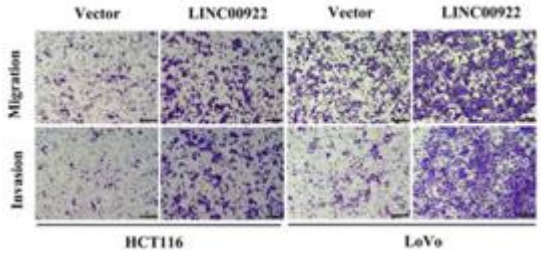

b)

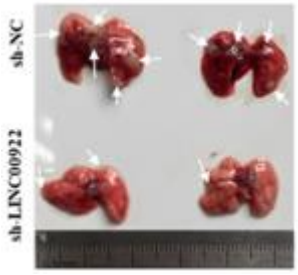

c)

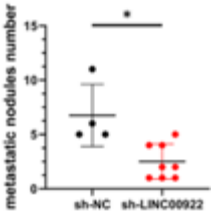

d)

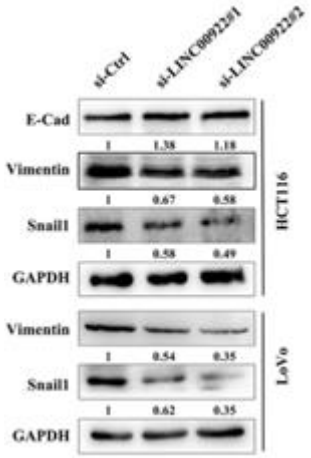

e)

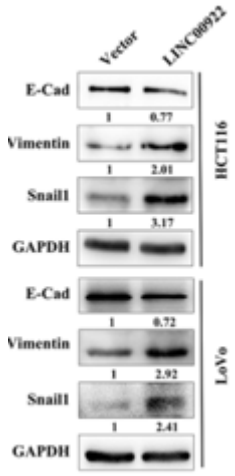

f)

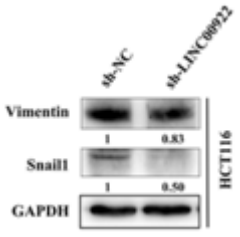

g)

Figure 3. LINC00922 promoted CRC metastasis

(a-b) Representative Transwell assay images illustrating the effects of transient LINC00922 knockdown (a) or overexpression (b) on invasion and migration of CRC

cells after 48 h. Scale bar, 200 μm. Quantification was performed by counting cells in three randomly chosen fields (middle panels). (C) Representative photographs of lung tissues showing metastatic foci arising from HCT116 cells with stable LINC00922 knockdown. Arrows mark the tumor nodules. (d) Quantitative analysis of the number of lung metastatic nodules in the sh-NC versus sh-LINC00922 experimental groups. (e-g) Immunoblotting results for E-Cad, Vimentin, Snail1, and GAPDH protein levels in CRC cells following transient knockdown (e), transient overexpression (f), or stable knockdown (g) of LINC00922. The numbers under each band indicate the relative protein/GAPDH ratio in the experimental conditions compared with controls, quantified using ImageJ2. Data are shown as means ± SD, * $P < 0.05$, ** $P < 0.01$, *** $P < 0.001$, **** $P < 0.0001$, unpaired two-tailed Student's t-test.

LINC00922 promotes invasion and migration via H3K27cr-mediated CAMs in epithelial cells

To ascertain whether LINC00922 influences CRC cell invasion and migration in an H3K27cr-dependent manner, stable LINC00922 knockdown cells were exposed to 10 mM NaCr for 48 h to reinstate H3K27cr levels. NaCr supplementation reversed the alterations in E-Cad, Vimentin, and Snail1 expression and fully recovered the invasive and migratory properties of the knockdown cells **(Figures 4a and 4b)**. These observations support the conclusion that LINC00922 controls CRC cell motility primarily by modulating H3K27cr.

ChIP-seq was subsequently performed on HCT116 cells engineered to overexpress LINC00922, employing an anti-H3K27cr antibody. This approach identified 21,253 peaks with differential occupancy (|fold-change| > 1.2, * $P < 0.05$) relative to control cells **(Figure 4c)**, indicating that LINC00922 alters the chromosomal distribution of H3K27cr. Pathway analysis using KEGG on genes linked to these peaks demonstrated prominent enrichment in processes associated with metastasis, notably focal adhesion and adherens junction pathways **(Figure 4d)**. Recognizing that histone crotonylation typically marks transcriptionally active promoters, 653 genes containing two promoter-proximal peaks were selected for in-depth examination.

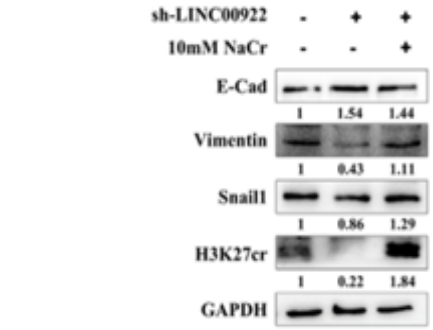

a)

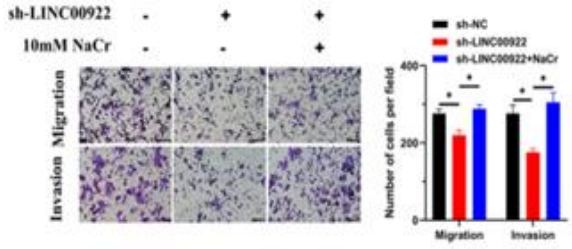

b)

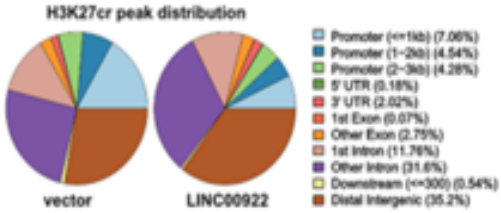

c)

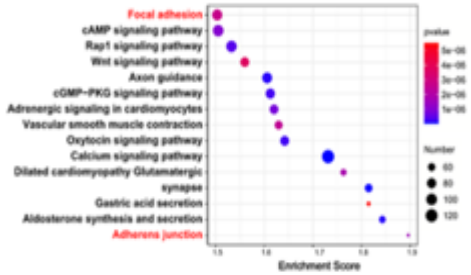

d)

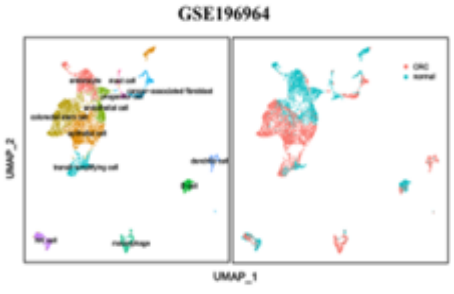

e)

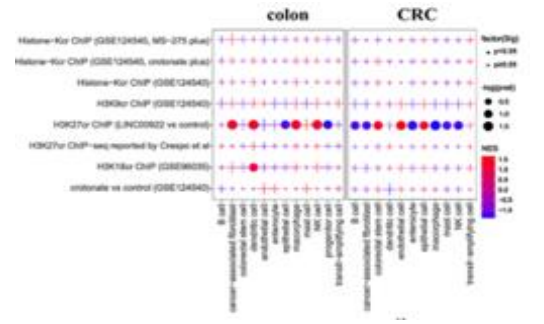

f)

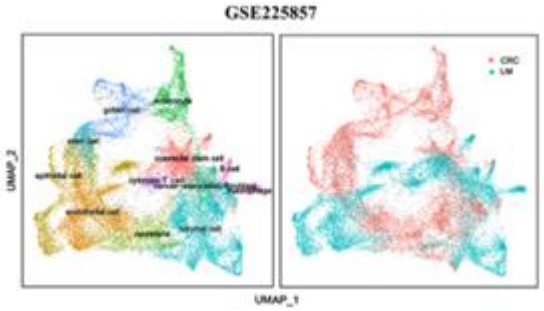

g)

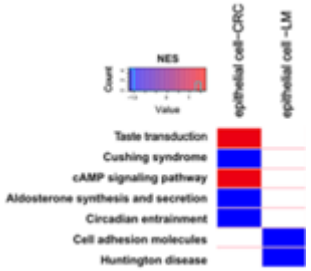

h)

Figure 4. LINC00922 promoted invasion and migration via H3K27cr-mediated CAMs in epithelial cells

(a) Western blot showing expression of E-Cad, Vimentin, and Snail1 proteins in stable LINC00922 knockdown HCT116 cells following 48 h treatment with 10 mM NaCr. Numbers under the bands denote the target protein/GAPDH ratio in experimental samples relative to controls, determined with ImageJ2. (b) Representative Transwell images of invasion and migration capacity in stable LINC00922 knockdown HCT116 cells treated with 10 mM NaCr for 48 h (left panel). Scale bar, 200 μm. Quantification was based on cell counts from three random microscopic fields (right panel). Data are expressed as means ± SD, $P < 0.05$, unpaired two-tailed Student's t-test, (c) Distribution of H3K27cr peaks across the genome in HCT116 cells transfected with LINC00922 overexpression or a control plasmid for 48 h, (d) KEGG pathway enrichment for genes associated with 21,253 differentially occupied H3K27cr peaks in HCT116 cells with or without transient LINC00922 overexpression for 48 h, (e) UMAP projection of single-cell transcriptomic data from CRC tissues (GSE196964). Colors distinguish cell lineages (left panel) or tissue categories (right panel). (f) GSEA-based enrichment of the 653 genes and related histone crotonylation gene sets in various cell populations of normal colon tissues (left panel) and CRC tissues (right panel). Dots signify * $P < 0.05$; plus symbols signify $P \geq 0.05$. Red dots indicate a positive association with the cell type, and blue dots indicate a negative association. Dot size reflects the negative base-10 logarithm of the p-value, (g) UMAP projection of single-cell transcriptomic profiles from CRC tissues (GSE225857). Colors represent different cell types (left panel) or tissue origins (right panel), and (H) Heatmap of pathway enrichment scores derived from the 653 genes in epithelial cells isolated from primary CRC and liver metastasis (LM) tissues. NES scores were computed via GSEA. Red denotes positive enrichment; blue denotes negative enrichment. LM: liver metastasis.

To define the cell populations most affected by LINC00922 through H3K27cr, the enrichment of the 653 genes was evaluated in single-cell transcriptomes of CRC samples using GSEA. Examination of 5,678 cells from dataset GSE196964 resolved 12 principal cell subtypes **(Figure 4e)**. In normal colon tissue, these genes were enriched in dendritic cells, cancer-associated fibroblasts, NK cells, macrophages, progenitor cells, and epithelial cells. Within CRC tissues, enrichment extended to nearly all cell types except dendritic cells and transit-amplifying cells **(Figure 4f)**.

A comparable analysis of the GSE221575 dataset, comprising 5,179 cells and 11 cell subtypes, showed strong enrichment for endothelial and epithelial cells in normal colon tissue. In CRC and liver metastasis tissues, the genes were predominantly enriched in B cells and epithelial cells. Consequently, epithelial cells became the primary focus of subsequent analyses.

Pathway annotation of the 653 genes identified 79 biological pathways each containing more than five associated genes, among which focal adhesion, adherens junction, tight junction, and cell adhesion molecules (CAMs) were prominent. Analysis of the GSE225857 dataset (20,753 cells, 12 subtypes); **(Figure 4g)** compared these pathways in epithelial cells from primary CRC versus liver metastasis (LM) tissues. The CAMs pathway exhibited negative enrichment specifically in

epithelial cells from LM tissues, but not in those from primary tumors **(Figure 4h)**. These results indicate that LINC00922 facilitates invasion and migration of CRC cells by regulating H3K27cr-dependent expression of cell adhesion molecules (CAMs) in epithelial cells.

LINC00922 promotes invasion and migration via ETS1

Earlier investigations have shown that the transcription factor ETS1 governs the expression of cell adhesion molecules. In light of this, the current study examined whether LINC00922 influences CRC cell invasion and migration via ETS1. Ectopic expression of ETS1 significantly enhanced invasion, migration, and overall motility in CRC cells **(Figures 5a and 5b)**. ETS1 overexpression also led to elevated levels of Vimentin and Snail1, along with reduced E-Cad expression **(Figure 5c)**. Rescue experiments further revealed that ETS1 inhibition reversed the enhanced motility and restored normal expression of EMT markers in LINC00922-overexpressing cells **(Figures 5d-5f)**. Taken together, these results establish ETS1 as an important downstream effector in the pathway by which LINC00922 drives invasive and migratory phenotypes.

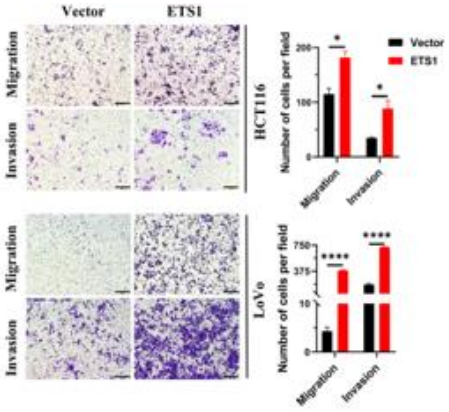

a)

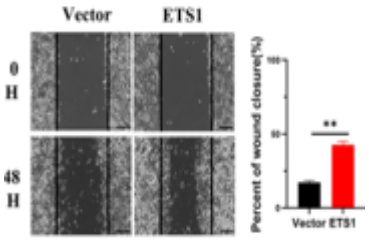

b)

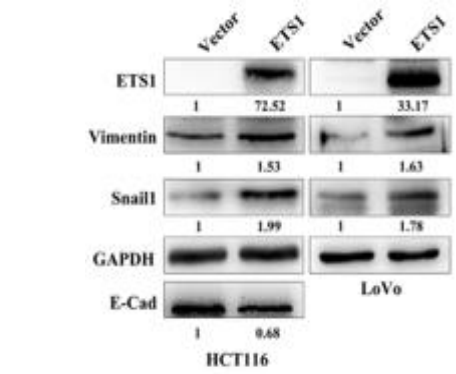

c)

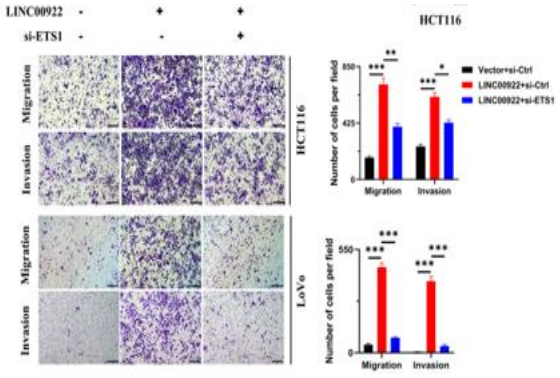

d)

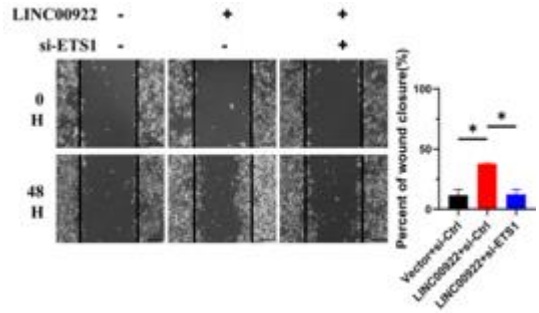

e)

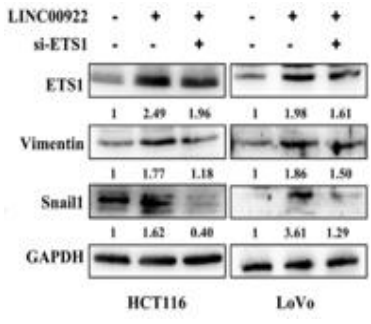

f)

Figure 5. LINC00922 promoted invasion and migration via ETS1

(a-b) Representative Transwell (a) and wound healing (b) assay images of cell motility following ETS1

overexpression for 48 h (left panels). Scale bar, 200 μm. Quantitative assessment of cell numbers and wound closure was performed in three random fields (right panels). (c) Western blot analysis showing levels of E-Cad, Vimentin, Snail1, ETS1, and GAPDH in CRC cells after transient ETS1 overexpression for 48 h. (d-e) Representative Transwell (d) and wound healing (e) assay images of cell motility in HCT116 cells simultaneously transfected with LINC00922 plasmid and si-ETS1 for 48 h (left panels). Scale bar, 200 μm. Cell counts and wound closure percentages were measured across three random fields (right panels), and (f) Western blot analysis of Vimentin, Snail1, ETS1, and GAPDH in CRC cells co-transfected with LINC00922 plasmid and si-ETS1 for 48 h. Numbers below the bands represent the ratio of each protein to GAPDH in experimental groups versus controls, as quantified by ImageJ2. Data are shown as means ± SD, * $P < 0.05$, ** $P < 0.01$, *** $P < 0.001$, **** $P < 0.0001$, unpaired two-tailed Student's t-test.

LINC00922 regulates ETS1 expression by modulating H3K27cr level

Whether LINC00922 affects ETS1 expression was subsequently examined. Quantitative RT-PCR performed on CRC tissue samples from 28 patients demonstrated a strong positive correlation between LINC00922 and ETS1 transcript abundance **(Figure 6a)**. Both transient and stable suppression of LINC00922 led to reduced ETS1 mRNA levels **(Figures 6b-6c)**, while LINC00922 overexpression elevated ETS1 mRNA **(Figure 6d)**. Parallel changes occurred at the protein level **(Figures 6e-6g)**. Immunofluorescence staining confirmed that stable LINC00922 knockdown caused a clear reduction in ETS1 protein **(Figure 6h)**.

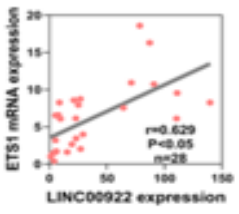

a)

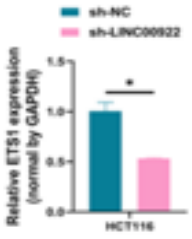

b)

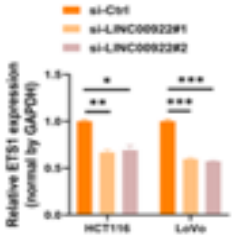

c)

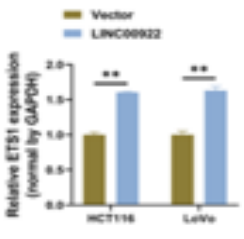

d)

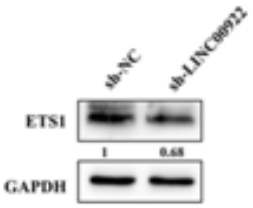

e)

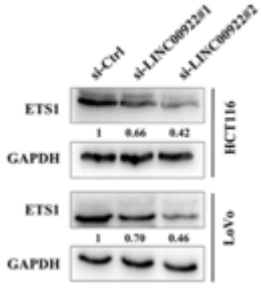

f)

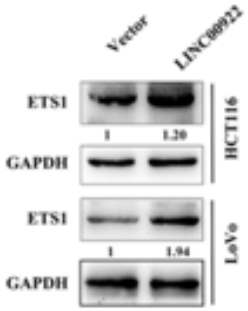

g)

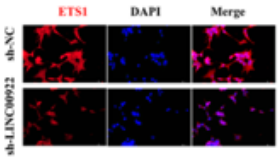

h)

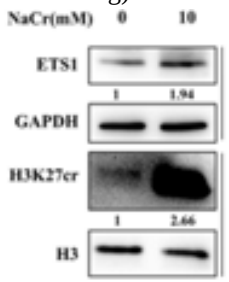

i)

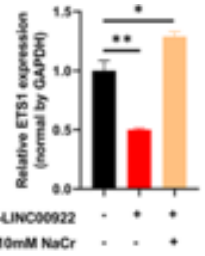

j)

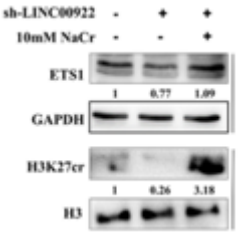

k)

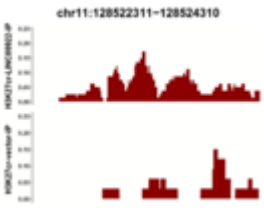

l)

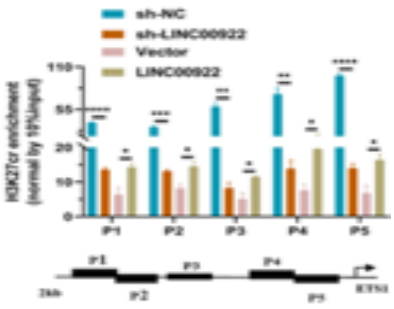

m

Figure 6. LINC00922 regulated ETS1 expression via H3K27cr

(a) qRT-PCR analysis of the correlation between LINC00922 and ETS1 expression in CRC tissues (n = 28). (b-g) qRT-PCR (b-d) and immunoblotting (e-g) analyses of ETS1 expression in HCT116 cells following stable LINC00922 knockdown (B, E), transient si-LINC00922 transfection (c, f), or LINC00922 plasmid transfection (d, g) for 48 h. (h) Immunofluorescence staining for ETS1 (red) in HCT116 cells with stable LINC00922 knockdown. Scale bar, 100 μm. (i) Immunoblotting of ETS1, H3K27cr, H3, and GAPDH in HCT116 cells treated with 10 mM NaCr for 48 h. (J-K) qRT-PCR (j) and immunoblotting (k) analyses of ETS1 expression in stable LINC00922 knockdown HCT116 cells after supplementation with 10 mM NaCr for 48 h, (l) Visualization of H3K27cr enrichment at the ETS1 promoter in HCT116 cells with transient LINC00922 overexpression for 48 h, (m) ChIP-qPCR quantification of H3K27cr occupancy at the ETS1 promoter in HCT116 cells subjected to stable LINC00922 knockdown or transient overexpression for 48 h. Numbers below western bands indicate the ratio of target protein versus GAPDH or H3 in experimental groups relative to controls, quantified using ImageJ2. Data are presented as means ± SD, * $P < 0.05$, ** $P < 0.01$, *** $P < 0.001$, **** $P < 0.0001$, unpaired two-tailed Student's t-test.

The mechanism linking LINC00922 to ETS1 regulation via H3K27cr was then addressed. Treatment of HCT116 cells with 10 mM NaCr elevated both H3K27cr and ETS1 levels, consistent with the idea that H3K27cr promotes ETS1 transcription **(Figure 6i)**. Importantly, supplementing NaCr to stable LINC00922 knockdown cells for 48 h restored ETS1 expression **(Figures 6j and 6k)**, demonstrating that LINC00922 controls ETS1 levels through H3K27cr modulation. Fractionation studies showed that LINC00922 predominantly localized to the nucleus. ChIP-seq analysis revealed enhanced H3K27cr occupancy at the ETS1 promoter following LINC00922 overexpression **(Figure 6l)**, a result corroborated by ChIP-qPCR experiments showing decreased promoter occupancy upon LINC00922 silencing and increased occupancy upon its overexpression **(Figure 6m)**. In summary, LINC00922 alters H3K27cr enrichment at the ETS1 promoter, thereby altering ETS1 expression.

LINC00922 modifies H3K27cr occupancy via interaction with SIRT3

This study explored the mechanism through which LINC00922 regulates the enrichment of H3K27cr at the ETS1 promoter. ChIP-seq performed in HCT116 cells indicated that SIRT3 occupies regions proximal to the transcription start site (TSS) **(Figure 7a)**. Nevertheless, the molecular details underlying SIRT3 recruitment to the TSS remain unresolved. It was postulated that LINC00922 facilitates the accumulation of SIRT3 at this site. To examine this possibility, the association between SIRT3 and H3K27cr was initially assessed in HCT116 cells. Immunofluorescence staining demonstrated nuclear co-localization of SIRT3 and H3K27cr in these cells **(Figure 7b)**. Consistent with expectations, ectopic expression of SIRT3 led to a reduction in H3K27cr abundance **(Figure 7c)**.

Further experiments examined whether LINC00922 affects H3K27cr occupancy by modulating SIRT3. RNA immunoprecipitation (RIP) assays confirmed a direct interaction between LINC00922 and SIRT3 in HCT116 cells, with markedly enhanced binding upon SIRT3 overexpression **(Figure 7d)**. Complementary RNA-FISH analysis verified the co-localization of LINC00922 transcripts with SIRT3 protein in the same cellular context **(Figure 7e)**. Additional RIP experiments also detected an interaction between LINC00922 and H3K27cr **(Figure 7f)**. Motif analysis of SIRT3 ChIP-seq data revealed a consensus binding sequence that was present within the ETS1 promoter.

ChIP-qPCR was subsequently employed to determine the impact of LINC00922 on SIRT3 recruitment to the ETS1 promoter. Knockdown of LINC00922 enhanced SIRT3 binding at this locus, whereas LINC00922 overexpression diminished it **(Figure 7g)**. A rescue experiment was then carried out by simultaneously transfecting SIRT3 and LINC00922 expression plasmids into HCT116 cells for 48 h. Overexpression of SIRT3 successfully restored ETS1 protein levels **(Figure 7h)**.

Collectively, these results establish that LINC00922 binds SIRT3 and promotes its dissociation from the ETS1 promoter, resulting in elevated H3K27cr levels at this site and subsequent activation of ETS1 transcription.

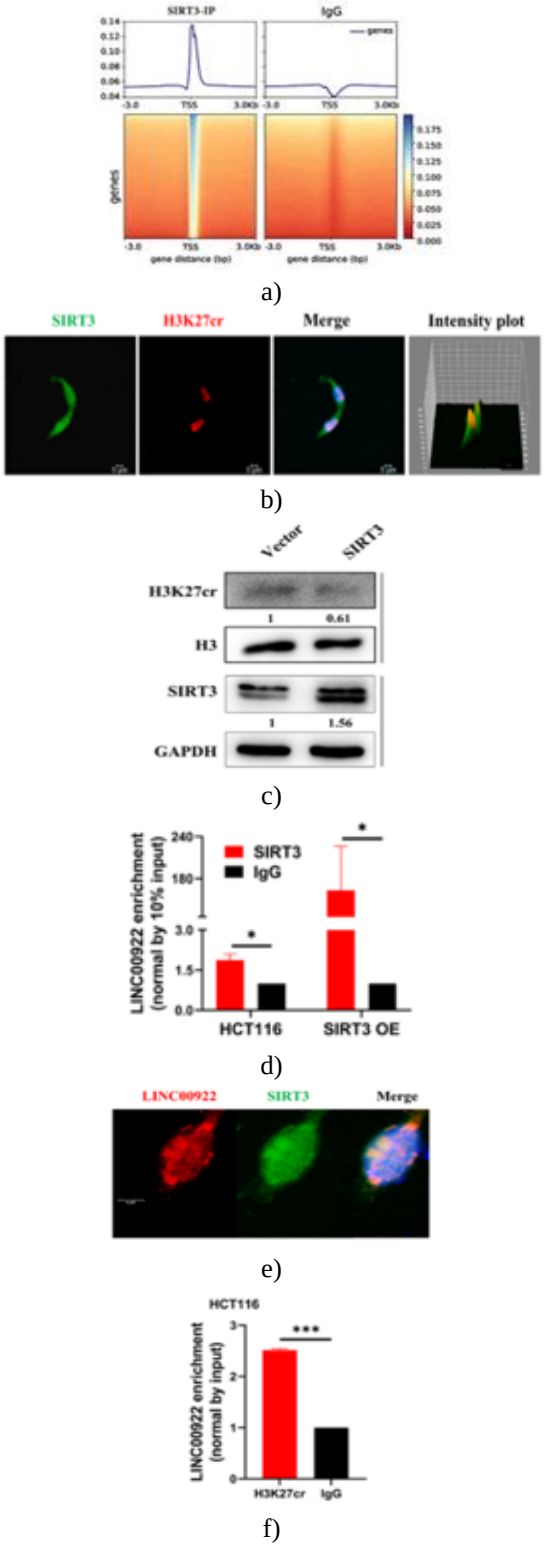

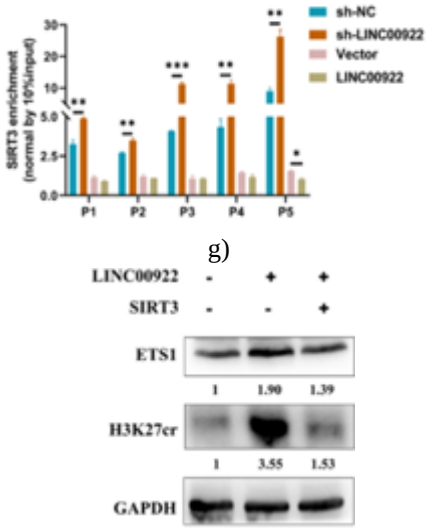

Figure 7. LINC00922 regulates H3K27cr occupancy through SIRT3

(a) Heatmaps and average signal density plots centered on transcriptional start sites of SIRT3 target genes, (b) Immunofluorescence images illustrating the nuclear distribution of SIRT3 (green) and H3K27cr (red) in HCT116 cells. Scale bar, 5 μm, (c) Western blot analysis of H3K27cr levels following transfection of HCT116 cells with a SIRT3 plasmid for 48 h, (d) RIP-qPCR quantification of LINC00922 enrichment with SIRT3 in HCT116 cells, with or without transient SIRT3 overexpression for 48 h ($n = 3$), (e) Combined RNA-FISH and immunofluorescence detection of LINC00922 RNA (red) and SIRT3 protein (green) in HCT116 cells. Scale bar, 5 μm, (f) RIP-qPCR assessment of LINC00922 interaction with H3K27cr in HCT116 cells, (g) ChIP-qPCR measurement of SIRT3 occupancy at the ETS1 promoter in HCT116 cells subjected to stable knockdown of LINC00922 or transient overexpression for 48 h ($n = 3$), and (h) Western blot analysis of ETS1 levels in HCT116 cells after co-transfection with LINC00922 and SIRT3 plasmids for 48 h. The numbers beneath the western blot bands denote the relative protein abundance normalized to GAPDH or H3, determined using ImageJ2. Data are shown as means ± SD, * $P < 0.05$, ** $P < 0.01$, *** $P < 0.001$, unpaired, two-tailed Student's t-test.

Clinical data reveal notable differences in lysine crotonylation (Kcr) abundance among diverse tumor entities. Earlier reports documented increased Kcr in multiple cancer types, including those of the colon,

prostate, thyroid, esophagus, pancreas, and lung. In contrast, decreased Kcr was observed in liver, stomach, and kidney malignancies [13, 25]. However, Zhang *et al*. [8] described a relative upregulation of Kcr in liver cancer specimens. The present analysis identified elevated H3K27cr in colorectal cancer (CRC) specimens relative to paired non-tumorous tissues, with progressive accumulation paralleling increasing tumor aggressiveness. LINC00922 transcript levels displayed a pattern similar to that of H3K27cr across these samples. Forced expression of LINC00922 produced a pronounced rise in H3K27cr abundance. This supports the notion that aberrant LINC00922 upregulation in CRC directly contributes to increased H3K27cr modification. Given the strong association of high LINC00922 expression with distant metastasis and lymph node involvement in CRC, the concomitant increase in H3K27cr at metastatic foci appears expected.

Knowledge concerning the link between Kcr and metastatic progression remains limited. Wan *et al*. [25] reported an association between Kcr abundance and TNM classification in hepatocellular carcinoma (HCC), noting that elevated Kcr suppressed cellular motility in HCC models. In contrast, site-specific crotonylation of non-histone targets, such as ENO1 at K420, has been found to drive invasive and migratory behavior in CRC cells [12]. Similarly, p300-dependent crotonylation of HNRNPA1 enhances invasion and migration in HeLa cells [26], while Kcr exerts comparable pro-migratory effects in prostate cancer cell lines [13]. In this study, H3K27cr levels exhibited a positive relationship with the M category in CRC clinical samples. Markedly higher H3K27cr was detected in tissues from distant metastases compared with primary tumors. Treatment with NaCr further augmented the invasive and metastatic capabilities of CRC cells. Gene ontology analysis of regions enriched for H3K27cr peaks implicated multiple pathways linked to metastatic dissemination. In particular, pronounced H3K27cr deposition at the ETS1 promoter stimulated ETS1 gene transcription, thereby facilitating cellular invasion and distant spread. Together, these observations confirm that H3K27cr promotes metastasis in CRC.

Prior research has largely focused on SIRT3's deacetylase activity, paying comparatively little attention to its ability to remove crotonyl groups. SIRT3 targets a diverse array of substrates for deacetylation, including histones and various non-histone proteins. Evidence from several groups suggests targeted recruitment of SIRT3 to defined chromatin domains. Iwahara *et al*. [27], for instance, showed that SIRT3 influences transcriptional programs by directly associating with chromatin at selected loci. In response to DNA double-strand breaks, SIRT3 localizes to damage sites and supports nonhomologous end-joining (NHEJ) repair by reducing H3K56ac [28]. During hepatitis B virus (HBV) infection, nuclear SIRT3 is directed to viral covalently closed circular DNA (cccDNA), where it represses transcription by altering histone H3 acetylation status [29]. Nevertheless, the regulatory processes governing SIRT3 tethering to and eviction from specific genomic sites remain poorly understood. The current results demonstrate that SIRT3 overexpression strongly diminishes H3K27cr levels, affirming its decrotonylase function. ChIP-seq profiling showed SIRT3 enrichment centered at transcription start sites (TSS), mirroring the distribution of H3K27cr. Importantly, LINC00922 physically associates with SIRT3 in HCT116 cells. Yet, elevated LINC00922 interferes with SIRT3 occupancy at the ETS1 promoter, leading to local accumulation of H3K27cr, ETS1 upregulation, and enhanced metastatic behavior.

Conclusion

The present work delineates a mechanistic framework describing how LINC00922 orchestrates SIRT3 recruitment and consequent H3K27cr modification to drive metastatic dissemination in human cancers. Deeper elucidation of histone crotonylation dynamics in pathophysiological contexts may open avenues for novel therapeutic interventions in oncology.

Acknowledgments: None

Conflict of Interest: None

Financial Support: None

Ethics Statement: None

References

1. Tan M, Luo H, Lee S, Jin F, Yang JS, Montellier E, et al. Identification of 67 histone marks and histone lysine crotonylation as a new type of histone modification. Cell. 2011;146(6):1016-28.
2. Fang Y, Xu X, Ding J, Yang L, Doan MT, Karmaus PWF, et al. Histone crotonylation promotes

mesoendodermal commitment of human embryonic stem cells. Cell Stem Cell. 2021;28(4):748-63.e7.
3. Liu S, Yu H, Liu Y, Liu X, Zhang Y, Bu C, et al. Chromodomain Protein CDYL Acts as a Crotonyl-CoA Hydratase to regulate histone crotonylation and spermatogenesis. Mol Cell. 2017;67(5):853-66.e5.
4. Wang J, Shen F, Liu F, Zhuang S. Histone modifications in Acute kidney Injury. Kidney Dis (Basel). 2022;8(6):466-77.
5. Jiang G, Nguyen D, Archin NM, Yukl SA, Méndez-Lagares G, Tang Y, et al. HIV latency is reversed by ACSS2-driven histone crotonylation. J Clin Invest. 2018;128(3):1190-8.
6. Zheng Z, Yan G, Li X, Fei Y, Sun L, Yu H, et al. Lysine crotonylation regulates leucine-deprivation-induced autophagy by a 14-3-3ε-PPM1B axis. Cell Rep. 2022;41(12):111850.
7. Yu H, Bu C, Liu Y, Gong T, Liu X, Liu S, et al. Global crotonylome reveals CDYL-regulated RPA1 crotonylation in homologous recombination-mediated DNA repair. Sci Adv. 2020;6(11):eaay4697.
8. Zhang D, Tang J, Xu Y, Huang X, Wang Y, Jin X, et al. Global crotonylome reveals hypoxia-mediated lamin a crotonylation regulated by HDAC6 in liver cancer. Cell Death Dis. 2022;13(8):717.
9. Fellows R, Denizot J, Stellato C, Cuomo A, Jain P, Stoyanova E, et al. Microbiota derived short chain fatty acids promote histone crotonylation in the colon through histone deacetylases. Nat Commun. 2018;9(1):105.
10. Ratajczak W, Rył A, Mizerski A, Walczakiewicz K, Sipak O, Laszczyńska M. Immunomodulatory potential of gut microbiome-derived short-chain fatty acids (SCFAs). Acta Biochim Pol. 2019;66(1):1-12.
11. Liao P, Bhattarai N, Cao B, Zhou X, Jung JH, Damera K, et al. Crotonylation at serine 46 impairs p53 activity. Biochem Biophys Res Commun. 2020;524(3):730-5.
12. Hou JY, Cao J, Gao LJ, Zhang FP, Shen J, Zhou L, et al. Upregulation of α enolase (ENO1) crotonylation in colorectal cancer and its promoting effect on cancer cell metastasis. Biochem Biophys Res Commun. 2021;578:77-83.
13. Xu X, Zhu X, Liu F, Lu W, Wang Y, Yu J. The effects of histone crotonylation and bromodomain protein 4 on prostate cancer cell lines. Transl Androl Urol. 2021;10(2):900-14.
14. Liao M, Chu W, Sun X, Zheng W, Gao S, Li D, et al. Reduction of H3K27cr modification during DNA damage in Colon cancer. Front Oncol. 2022;12:924061.
15. Wei W, Liu X, Chen J, Gao S, Lu L, Zhang H, et al. Class I histone deacetylases are major histone decrotonylases: evidence for critical and broad function of histone crotonylation in transcription. Cell Res. 2017;27(7):898-915.
16. Bao X, Wang Y, Li X, Li XM, Liu Z, Yang T, et al. Identification of 'erasers' for lysine crotonylated histone marks using a chemical proteomics approach. Elife. 2014;3.
17. Liao W, Xu N, Zhang H, Liao W, Wang Y, Wang S, et al. Persistent high glucose induced EPB41L4A-AS1 inhibits glucose uptake via GCN5 mediating crotonylation and acetylation of histones and non-histones. Clin Transl Med. 2022;12(2):e699.
18. Wang Z, Zhao Y, Xu N, Zhang S, Wang S, Mao Y, et al. NEAT1 regulates neuroglial cell mediating Aβ clearance via the epigenetic regulation of endocytosis-related genes expression. Cell Mol Life Sci. 2019;76(15):3005-18.
19. Wang Y, Dong T, Wang P, Li S, Wu G, Zhou J, et al. LINC00922 regulates epithelial-mesenchymal transition, invasive and migratory capacities in breast cancer through promoting NKD2 methylation. Cell Signal. 2021;77:109808.
20. Zhang C, Wang L, Jin C, Zhou J, Peng C, Wang Y, et al. Long non-coding RNA Lnc-LALC facilitates colorectal cancer liver metastasis via epigenetically silencing LZTS1. Cell Death Dis. 2021;12(2):224.
21. Korotkevich G, Sukhov V, Budin N, Shpak B, Artyomov MN, Sergushichev A. Fast Gene Set Enrichment Analysis. bioRxiv. 2016;060012. [Preprint].
22. Robinson MD, McCarthy DJ, Smyth GK. edgeR: a Bioconductor package for differential expression analysis of digital gene expression data. Bioinformatics. 2010;26(1):139-40.
23. Wu D, Bi X, Li P, Xu D, Qiu J, Li K, et al. Enhanced insulin-regulated phagocytic activities support extreme health span and longevity in multiple populations. Aging Cell. 2023;22(5):e13810.
24. Sabari BR, Tang Z, Huang H, Yong-Gonzalez V, Molina H, Kong HE, et al. Intracellular crotonyl-CoA stimulates transcription through p300-catalyzed histone crotonylation. Mol Cell. 2015;58(2):203-15.

25. Wan J, Liu H, Ming L. Lysine crotonylation is involved in hepatocellular carcinoma progression. Biomed Pharmacother. 2019;111:976-82.
26. Han X, Xiang X, Yang H, Zhang H, Liang S, Wei J, et al. p300-Catalyzed Lysine Crotonylation Promotes the Proliferation, Invasion, and Migration of HeLa Cells via Heterogeneous Nuclear Ribonucleoprotein A1. Anal Cell Pathol (Amst). 2020;2020:5632342.
27. Iwahara T, Bonasio R, Narendra V, Reinberg D. SIRT3 functions in the nucleus in the control of stress-related gene expression. Mol Cell Biol. 2012;32(24):5022-34.
28. Sengupta A, Haldar D. Human sirtuin 3 (SIRT3) deacetylates histone H3 lysine 56 to promote nonhomologous end joining repair. DNA Repair (Amst). 2018;61:1-16.
29. Ren JH, Hu JL, Cheng ST, Yu HB, Wong VKW, Law BYK, et al. SIRT3 restricts hepatitis B virus transcription and replication through epigenetic regulation of covalently closed circular DNA involving suppressor of variegation 3–9 homolog 1 and SET domain containing 1A histone methyltransferases. Hepatology. 2018;68(4):1260-76.